6th International Conference on Multiphase Flow,
ICMF 2007, Leipzig, Germany, July 9 – 13, 2007

# Comparison between Euler/Euler and Euler/Lagrange LES approaches for confined bluff-body gas-solid flow prediction

Marta García[1], Eleonore Riber[1,2], Olivier Simonin[2] and Thierry Poinsot[2]

[1] CERFACS, 42, av. Gaspard Coriolis, Toulouse, 31057, France

[2] IMF Toulouse, UMR CNRS/INPT/UPS, Allée du Professeur Camille Soula, Toulouse, 31400, France

garcia@cerfacs.fr, riber@cerfacs.fr, simonin@imft.fr, poinsot@imft.fr

**Keywords**: Large-eddy simulation, gas-solid flows, bluff-body flow, Eulerian and Lagrangian approaches

## Abstract

In this study, Euler/Euler and Euler/Lagrange LES predictions of particle-laden turbulent flows are compared for the bluff-body configuration from Borée *et al.* (2001) where glass beads are injected into a complex recirculating flow. These tests are performed for non-reacting, non-evaporating sprays but are mandatory validations before computing realistic combustion chambers. The numerical code used for this study is a parallel explicit CFD code that solves the 3D compressible Navier-Stokes equations on unstructured and hybrid grids. This solver contains both Euler/Euler and Euler/Lagrange formulations. Results show that the gas flow and the dispersed phase are well predicted but the Lagrangian approach predicts RMS values more precisely. The importance of inlet boundary conditions for the gas is revealed.

## Introduction

Today, RANS (Reynolds-averaged Navier-Stokes) equations are routinely solved to design combustion chambers, for both gaseous and liquid fuels. Recently, in order to provide better accuracy for the prediction of mean flows but also to give access to unsteady phenomena occurring in combustion devices (such as instabilities, flashback or quenching), Large-Eddy Simulation (LES) has been extended to reacting flows. The success of these approaches for gaseous flames in the last years (Caraeni *et al.* 2000; Colin *et al.* 2000; Selle *et al.* 2004; Roux *et al.* 2005; Poinsot & Veynante 2005) is a clear illustration of their potential. LES gives access to the large scales structures of the flow reducing the importance of modelling, and naturally capturing a significant part of the physics controlling these flames. Even though LES has already demonstrated its potential for gaseous flames, its extension to two-phase flames is still largely to be done. First, the physical submodels required to describe the atomization of a liquid fuel jet, the dispersion of solid particles, their interaction with walls, evaporation and combustion are as difficult to build in LES as in RANS because they are essentially subgrid phenomena. Second, the numerical implementation of two-phase flow LES remains a challenge. The equations for both the gaseous and the dispersed phases must be solved together at each time step in a strongly coupled manner. This differs from classical RANS where the resolution of the two phases can be done in a weak procedure, bringing first the gas flow to convergence, then the solid particles and finally iterating until convergence of both phases. Finally, in the context of parallel super-computing, numerical efficiency is an additional constraint. For single-phase flows, efficient and accurate solvers have been developed and speedups of the order of $5000$ are not uncommon (http://www.cerfacs.fr/cfd/parallel.html). Maintaining a similar parallel efficiency for a two-phase flow solver while representing the main physics of the flow raises additional questions.

In LES of two-phase flows, physics and numerics interact strongly: the first question is to choose a paradigm to describe the two-phase flow. Most RANS codes use Euler/Lagrange (EL) methods in which the flow is solved using an Eulerian method and the particles are tracked using a Lagrangian approach. An alternative technique is to use two-fluid models in which both the gas and the dispersed phases are solved using an Eulerian method (Euler/Euler or EE) (Reeks 1991; Février & Simonin 1999). The history of RANS development has shown that both EE and EL are useful and either is found today in most commercial codes. For LES, both EE and EL formulations are being developed and the focus of this study is to test them in a reference case where complete sets of solutions for gas and dispersed phase are available. This exercice is performed here without evaporation or combustion.

## Nomenclature

| | |
|---|---|
| $C_D$ | drag coefficient |
| $C_I, C_S$ | model constants |
| $C_v$ | specific heat at constant volume ($J\ kg^{-1}\ K^{-1}$) |
| $d_p$ | particle diameter ($m$) |
| $e_g$ | internal energy ($m^2\ s^{-2}$) |
| $E_g$ | total energy ($m^2\ s^{-2}$) |
| $f_{c,i}$ | coupling force ($kg\ m^{-2}\ s^{-2}$) |

| | |
|---|---|
| $\breve{f}_p$ | probability density function ($s^3\ m^{-6}$) |
| g | gravitational constant ($m\ s^{-2}$) |
| $n_p$ | particle number density ($m^{-3}$) |
| $N_{procs}$ | number of processors |
| $p$ | pressure ($N\ m^{-2}$) |
| $Pr$ | Prandtl number |
| $q_{g,j}$ | heat tranfer vector ($J\ m^{-2}\ s^{-1}$) |
| $q_{gp,SGS}$ | subgrid covariance ($m^{-2}\ s^{-2}$) |
| $Q$ | diffusion term ($J\ m^{-2}\ s^{-1}$) |
| $\mathcal{R}$ | air gas constant ($J\ kg^{-1}\ K^{-1}$) |
| $r$ | radial direction ($m$) |
| $Re$ | Reynolds number |
| $S$ | strain rate tensor ($s^{-1}$) |
| t | time ($s$) |
| $T$ | temperature ($K$) |
| $\mathcal{T}$ | stress tensor ($kg\ m^{-1}\ s^{-2}$) |
| $u_i$ | velocity vector, i=1,2,3 ($m\ s^{-1}$) |
| $\mathrm{v}_r$ | local instantaneous relative velocity ($m\ s^{-1}$) |
| $x_i$ | position vector, i=1,2,3 ($m$) |
| $z$ | axial direction ($m$) |

*Greek letters*

| | |
|---|---|
| $\alpha$ | volume fraction |
| $\delta_{ij}$ | Kronecker delta |
| $\delta\theta_p$ | Random Uncorrelated Energy (RUE) ($m^2\ s^{-2}$) |
| $\delta R_{p,ij}$ | Random Uncorrelated Velocity (RUV) tensor ($m^2 s^{-2}$) |
| $\delta S_{p,iij}$ | RUV third correlation tensor ($m^{-3}\ s^{-3}$) |
| $\Delta_f$ | filter characteristic length ($m$) |
| $\eta$ | dynamic viscosity ($kg\ m^{-1}\ s^{-1}$) |
| $\kappa$ | diffusion coefficient ($m^2\ s^{-1}$) |
| $\nu$ | kinematic viscosity ($m^2\ s^{-1}$) |
| $\Pi_{\delta\theta_p}$ | production term by subgrid scales ($m^{-1}\ s^{-3}$) |
| $\rho$ | density ($kg\ m^{-3}$) |
| $\tau_p$ | particle relaxation time ($s$) |
| $\tau_{g,ij}$ | viscous stress tensor ($kg\ m^{-1}\ s^{-2}$) |
| $\phi$ | azimuthal direction ($m$) |

*Subscripts*

| | |
|---|---|
| g | gas phase |
| i,j,k | index of coordinates directions |
| p | particle (dispersed phase) |
| RUM | Random Uncorrelated Motion |
| SGS | subgrid-scale |

*Symbols*

| | |
|---|---|
| $\bar{\cdot}$ | LES-filtered quantity |
| $\tilde{\cdot}$ | gas Favre LES-filtered quantity |
| $\hat{\cdot}$ | particle Favre LES-filtered quantity |
| $\breve{\cdot}$ | mesoscopic quantity |

## Configuration and work objectives

In the present study, two approaches developed at CERFACS within the same solver are used to investigate some critical issues for LES of two-phase flows on massively parallel computers. The explicit compressible solver AVBP is used with both EE (Kaufmann *et al.* 2003) and EL formulations on the same tetrahedron-based grid.

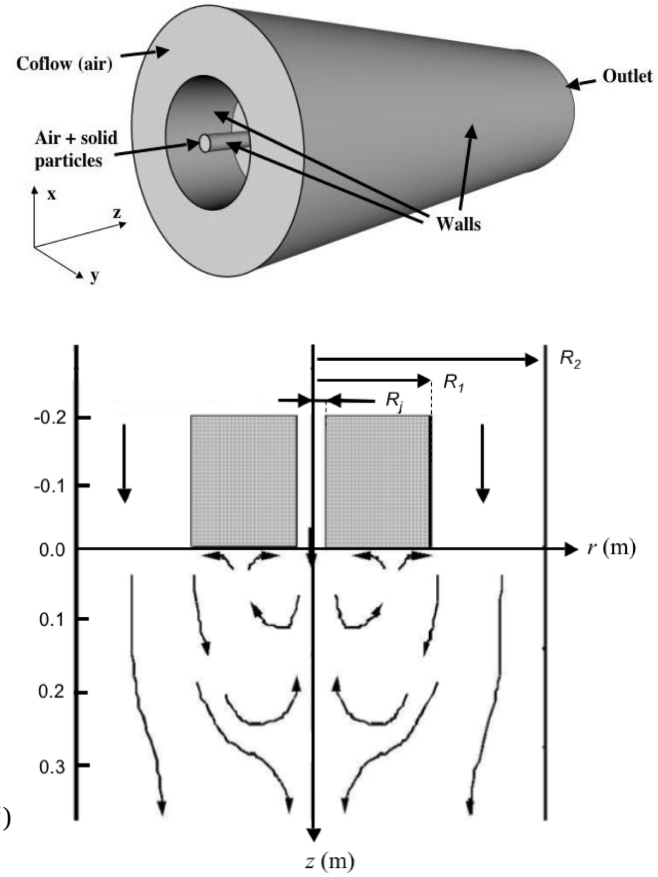


Figure 1: Configuration of Borée *et al.* (2001). The dimensions are : $R_j = 10$ mm, $R_1 = 75$ mm, $R_2 = 150$ mm. The total length of the experiment is $1.5$ m.

Both approaches are used to study a bluff-body configuration (Borée *et al.* 2001) where a jet of air and solid particles are injected in a coflow of air (see the sketch in Fig. 1). The jet velocity on the axis is $4$ m/s and the maximum coflow velocity is $6$ m/s. The experiment is designed to provide large recirculation zones between the central jet and the coflow. The dispersed phase consists of solid particles (glass beads with diameter ranging from 20 to 100 microns with a mean value of 60 microns) so that evaporation, coalescence and break up do not have to be considered. The material density of the glass particle is $\rho_p = 2470$ kg m$^{-3}$. The mass loading ratio of particles in the inner jet is 0.22 corresponding to a solid volume fraction smaller than $10^{-4}$. Thus collision effects are assumed to be negligible in the modelling approaches.

Measurements are performed by a two-component phase-Doppler anemometer (PDA). The origin is set at the edge of the bluff body and at the centre of the inner jet (see Fig. 1). The flow will be described using a cylindrical coordinate system $(z, r, \phi)$ to indicate the axial (downward), radial and azimuthal directions. Single-phase data are provided in tabulated form at different cross-sections within the jet, in the annular direction and along the $z$ axis. The radial profiles of mean and RMS particle velocities for each size classes are provided in tabulated form at 7 cross-sections of the $z$ axis ($z = 3, 80, 160, 200, 240, 320$ and $400$ mm) and along the $z$ axis up to $500$ mm. The complete data set, including

accurate boundary conditions, at moderate mass loading (22 percent) has been selected for benchmarking at the 'Ninth workshop on two-phase flow predictions' (Ishima *et al.* 1999) and can be obtained at the following web site: http://www-mvt.iw.uni-halle.de/english/index.php?bluff_body_flow.
Despite of the relative simplicity, this test case contains a number of issues relevant for LES of two-phase flows. These include (i) the comparison of performances and CPU cost for EE and EL approaches and (ii) the analysis of the inlet boundary condition on the dispersed phase solution (turbulent modulation).

## Description of the solver

The AVBP solver is a finite volume code based on a cell-vertex formulation. It solves the laminar and turbulent compressible Navier-Stokes equations in two and three space dimensions for hybrid and unstructured grids. Steady state or unsteady flows can be simulated, furthermore it takes into account the variations of molecular weights and heat capacities with temperature and mixture composition. A third-order scheme for spatial differencing and a Runge-Kutta time advancement (Colin & Rudgyard 2000; Moureau *et al.* 2005) is used for the present work. The Smagorinsky model is used to model the subgrid stress tensor. Walls are treated using the law-of-the-wall formulation by Schmitt *et al.* (2007). The boundary conditions are handled with the NSCBC formulation (Poinsot & Veynante 2005; Moureau *et al.* 2005).

The following sections briefly describe the governing equations solved by AVBP for the gaseous and dispersed phases.

## Gaseous phase

The filtered conservation equation for gas-phase density, $\bar{\rho}_g$, momentum, $\tilde{u}_{g,i}$, and total energy $\tilde{E}_g = \tilde{e}_g + \frac{1}{2}\tilde{u}_{g,j}^2$ (with $\tilde{e}_g = C_v\tilde{T}_g$, the internal energy, $C_v$ the specific heat at constant volume and $\tilde{T}_g$ the temperature) read:

$$\frac{\partial\bar{\rho}_g}{\partial t} + \frac{\partial(\bar{\rho}_g\tilde{u}_{g,j})}{\partial x_j} = 0 \tag{1}$$

$$\frac{\partial(\bar{\rho}_g\tilde{u}_{g,i})}{\partial t} + \frac{\partial(\bar{\rho}_g\tilde{u}_{g,i}\tilde{u}_{g,j})}{\partial x_j} + \frac{\partial\bar{p}_g}{\partial x_i} - \frac{\partial\bar{\tau}_{g,ij}}{\partial x_j} = \frac{\partial\mathcal{T}_{g,ij}}{\partial x_j} + f_{c,i} \tag{2}$$

$$\frac{\partial(\bar{\rho}_g\tilde{E}_g)}{\partial t} + \frac{\partial(\tilde{u}_{g,j}(\bar{\rho}_g\tilde{E}_g + \bar{p}_g))}{\partial x_j} - \frac{\partial(\bar{\tau}_{g,ij}\tilde{u}_{g,i})}{\partial x_j} + \frac{\partial\bar{q}_{g,j}}{\partial x_j} = \frac{\partial(\mathcal{T}_{g,ij}\tilde{u}_{g,i})}{\partial x_j} + \frac{\partial Q_{g,j}}{\partial x_j} + f_{c,j}\tilde{u}_{g,j}. \tag{3}$$

The left-hand-side (LHS) of Eqs. 1-3 contains all resolved (filtered) variables (being $\bar{\tau}_{g,ij}$ and $\bar{q}_{g,i}$ the viscous stress tensor and the heat transfer vector, while pressure is obtained from the equation of state $\bar{p}_g = \bar{\rho}_g\mathcal{R}\tilde{T}_g$). The right-hand-side (RHS) of Eqs. 2 and 3 contains the SGS terms $\mathcal{T}_{g,ij}$ and $Q_{g,i}$, which are reconstructed using eddy-viscosity concepts (with turbulent viscosity obtained from Smagorinsky model). The last terms in Eqs. 2 and 3, $f_{c,i}$ and $f_{c,j}\tilde{u}_{g,j}$, denote respectively, the coupling force and energy applied to the fluid by all particles.

## Dispersed phase: Euler/Lagrange approach

The dispersed phase consists of particles which are assumed to be rigid spheres with diameter comparable or smaller than the Kolmogorov length scale. As the particle density is much larger than the fluid density ($\rho_p/\rho_g = 2470$), the forces acting on particles reduce to drag and gravity. Under these assumptions, the particle equations of motion can then be written for a single particle as:

$$\frac{dx_{p,i}}{dt} = u_{p,i} \tag{4}$$

$$\frac{du_{p,i}}{dt} = -\frac{3}{4}\frac{\rho_g}{\rho_p}\frac{C_D}{d_p}\left|\mathbf{v}_r\right|\mathrm{v}_{r,i} + g_i = -\frac{u_{p,i} - \tilde{u}_{g,i}}{\tau_p} + g_i \tag{5}$$

with $g_i$ the gravity vector. The local drag coefficient in Eq. (5) is $C_D$ and may be expressed in terms of the particle Reynolds number $Re_p$ following Schiller & Nauman (1935):

$$C_D = \frac{24}{Re_p}\left[1 + 0.15Re_p^{0.687}\right] \tag{6}$$

$$Re_p = \frac{\left|\mathbf{v}_r\right| d_p}{\nu_g} \leq 800 \tag{7}$$

where $d_p$ is the particle diameter and $\nu_g$ is the kinematic viscosity of the gas phase. The local instantaneous relative velocity between the particle and the surrounding fluid is $\mathrm{v}_{r,i} = u_{p,i} - \tilde{u}_{g,i}$, where $\tilde{u}_{g,i}$ is the fluid velocity at the position of the particle assuming that the flow field is locally undisturbed by the presence of this particle (Gatignol 1983; Maxey & Riley 1983). In first approximation, the velocity is assumed to be equal to the interpolation of the filtered velocity at the position of the particle (Wang & Squires 1996; Yamamoto *et al.* 2001; Apte *et al.* 2003). The effect of the subgrid fluid turbulence is assumed to be negligible owing to the large inertia of the solid particles (Fede & Simonin 2006). The particle relaxation time $\tau_p$ is defined as the Stokes characteristic time:

$$\tau_p = \frac{4}{3}\frac{\rho_p}{\rho_g}\frac{d_p}{C_D\left|\mathbf{v}_r\right|}. \tag{8}$$

The influence of the particles on the gas phase is taken into account in the EL simulations by using the point-force approximation in the general framework of the particle-in-cell method (PIC) (Boivin *et al.* 1998; Vermorel *et al.* 2003), with standard single-phase subgrid turbulence modelling approaches. According to Boivin *et al.* (2000), such an assumption is valid for small mass loading ratio of particles (typically, $\alpha_p\rho_p/\rho_g \leq 1$) with response time larger than the subgrid turbulence characteristic time scale. Modification

of the gas subgrid-scale turbulence model by the particles is neglected. A linear interpolation algorithm is used to compute the fluid velocity at the position of the particle. If particle relaxation time is much larger than the time scale of filtered velocity fluctuations (as in the present case of 22 percent mass loading), such a linear interpolation is found to be sufficiently accurate to resolve particle motions (see e.g. Fede & Simonin (2006)).

### Dispersed phase: Euler/Euler approach

Eulerian equations for the dispersed phase can be derived using several approaches. A popular and simple way consists in volume filtering of the separate, local, instantaneous phase equations accounting for the inter-facial jump conditions (Druzhinin & Elghobashi 1999). Such an averaging approach is restrictive because particle sizes and particle distances have to be smaller than the smallest length scale of the turbulence. Besides, they do not account for the crossing of particle trajectories or Random Uncorrelated Motion (RUM), shown by Février *et al.* (2005), which may appear when the particle relaxation time is larger than the Kolmogorov time scale. In the present study, a statistical approach analogous to kinetic theory (Chapman & Cowling 1939) is used to construct a probability density function (pdf) $\breve{f}_p(\mathbf{c}_p, \mathbf{x}, t)$ which gives the local instantaneous probable number of particles with the given translation velocity $\mathbf{u}_p = \mathbf{c}_p$. The resulting model (Février *et al.* 2005; Moreau *et al.* 2005) leads to equations for the particle number density $\bar{n}_p$ and the correlated velocity $\hat{\mathbf{u}}_p$:

$$\frac{\partial}{\partial t}\bar{n}_p + \frac{\partial}{\partial x_j}\bar{n}_p\hat{u}_{p,j} = 0 \tag{9}$$

$$\frac{\partial}{\partial t}\bar{n}_p\hat{u}_{p,i} + \frac{\partial}{\partial x_j}\bar{n}_p\hat{u}_{p,i}\hat{u}_{p,j} = -\frac{\bar{n}_p}{\tau_p}\left(\hat{u}_{p,i} - \hat{u}_{g,i}\right)$$
$$+\bar{n}_p g_i - \frac{\partial}{\partial x_j}\mathcal{T}_{p,ij} - \frac{\partial}{\partial x_j}\bar{n}_p\widehat{\delta R}^*_{p,ij} - \frac{\partial}{\partial x_i}\frac{2}{3}\bar{n}_p\widehat{\delta\theta}_p \tag{10}$$

where $\bar{n}_p$, $\hat{\mathbf{u}}_p$ and $\widehat{\delta\theta}_p$ are respectively the filtered particle number density, correlated velocity and Random Uncorrelated Energy (RUE). The two first terms of the RHS of Eq. (10) are the drag force and gravity effects on large scales, the third one accounts for the subgrid-scale (SGS) effects, the fourth one takes into account the dissipation effects induced by the RUM and the last one is a particle-pressure term proportional to the RUE. $\mathcal{T}_{p,ij}$ stands for the particle subgrid stress tensor:

$$\mathcal{T}_{p,ij} = \bar{n}_p(\widehat{u_{p,i}u_{p,j}} - \hat{u}_{p,i}\hat{u}_{p,j}). \tag{11}$$

As in fluid non-isotherm turbulence, an additional equation for energy is needed. The transport equation of filtered RUE is:

$$\frac{\partial}{\partial t}\overline{n}_p\widehat{\delta\theta}_p + \frac{\partial}{\partial x_j}\overline{n}_p\hat{u}_{p,j}\widehat{\delta\theta}_p = -2\frac{\overline{n}_p}{\tau_p}\widehat{\delta\theta}_p - \frac{2}{3}\overline{n}_p\widehat{\delta\theta}_p\frac{\partial\hat{u}_{p,j}}{\partial x_j}$$

$$-\overline{n}_p\widehat{\delta R}^*_{p,ij}\frac{\partial\hat{u}_{p,i}}{\partial x_j} - \frac{1}{2}\frac{\partial}{\partial x_j}\overline{n}_p\widehat{\delta S}_{p,iij} + \Pi_{\delta\theta_p} - \frac{\partial}{\partial x_j}Q_{p,j}. \tag{12}$$

The first RHS term is the RUE destruction by drag force, the second one is a RUE-dilatation term, the third one is a production term by filtered Random Uncorrelated Velocity (RUV) tensor, the next one is the diffusion by filtered RUV third correlation tensor. $\Pi_{\delta\theta_p}$ and $Q_{p,j}$ are respectively production and diffusion terms by subgrid scales:

$$\Pi_{\delta\theta_p} = \left(\overline{\breve{n}_p\delta R_{p,ij}\frac{\partial\breve{u}_{p,i}}{\partial x_j}} - \bar{n}_p\widehat{\delta R}_{p,ij}\frac{\partial\hat{u}_{p,i}}{\partial x_j}\right) \tag{13}$$

$$Q_{p,j} = \bar{n}_p\left(\widehat{u_{p,j}\delta\theta}_p - \hat{u}_{p,j}\widehat{\delta\theta}_p\right). \tag{14}$$

The particle source term in the gas phase momentum Eq. 2 is equal to minus the drag term in the particle phase Eq. 10.

### Closure of filtered RUV terms

Assuming small anisotropy of the RUM, Simonin *et al.* (2002) model $\delta R^*_{p,ij}$ by a viscous term and Kaufmann *et al.* (2005) model $\delta S_{p,iij}$ by a diffusive term similar to Fick's law. For LES approach these models are adapted by replacing non filtered quantities by filtered ones leading to (Moreau *et al.* 2005):

$$\widehat{\delta R}^*_{p,ij} = -\hat{\nu}_{RUM}\left(\frac{\partial\hat{u}_{p,i}}{\partial x_j} + \frac{\partial\hat{u}_{p,j}}{\partial x_i} - \frac{\partial\hat{u}_{p,k}}{\partial x_k}\frac{\delta_{ij}}{3}\right) \tag{15}$$

$$\frac{1}{2}\widehat{\delta S}_{p,iij} = -\hat{\kappa}_{RUM}\frac{\partial\widehat{\delta\theta}_p}{\partial x_j} \tag{16}$$

where the RUM viscosity, $\hat{\nu}_{RUM}$, and the RUM diffusion coefficient, $\hat{\kappa}_{RUM}$, are given by:

$$\hat{\nu}_{RUM} = \frac{\tau_p}{3}\widehat{\delta\theta}_p \quad \text{and} \quad \hat{\kappa}_{RUM} = \frac{10}{27}\tau_p\widehat{\delta\theta}_p. \tag{17}$$

### Subgrid terms modeling

By analogy to single phase flows (Moin *et al.* 1991; Vreman *et al.* 1995), Riber *et al.* (2005) propose a viscosity model for the SGS tensor $\mathcal{T}_{p,ij}$. The trace-free SGS tensor is modeled using a viscosity assumption (compressible Smagorinsky model), while the subgrid energy is parametrized by a Yoshizawa model (Yoshizawa 1986):

$$\mathcal{T}_{p,ij} = -C_S 2\Delta_f^2\bar{n}_p|\hat{S}_p|(\hat{S}_{p,ij} - \frac{\delta_{ij}}{3}\hat{S}_{p,kk})$$
$$+ C_I 2\Delta_f^2\bar{n}_p|\hat{S}_p|^2\delta_{ij} \tag{18}$$

where $\hat{S}_p$ is the filtered particle strain rate tensor, $|\hat{S}_p|^2 = 2S_{p,ij}S_{p,ij}$ and $\Delta_f$ the filter characteristic length. The model constants have been evaluated in a priori tests (Riber *et al.* 2006) leading to the values $C_S = 0.02$, $C_I = 0.012$.
The subgrid diffusion term in the filtered RUE is modeled by an eddy-diffusivity model:

$$Q_{p,j} = -\frac{\bar{n}_p C_S 2\Delta_f^2|\hat{S}_p|}{Pr_{p,SGS}}\frac{\partial\widehat{\delta\theta}_p}{\partial x_j} \tag{19}$$

with the particle turbulent Prandtl number $Pr_{p,SGS} = 0.8$. The subgrid production of filtered RUE term $\Pi_{\delta\theta_p}$ acts like a dissipation term in the subgrid energy equation. Using an

equilibrium assumption on the particle correlated subgrid energy and neglecting diffusion terms leads to:

$$-\frac{\bar{n}_p}{\tau_p}\left(\frac{\mathcal{T}_{p,kk}}{\bar{n}_p} - q_{gp,SGS}\right) + \Pi_{\delta\theta_p} - \mathcal{T}_{p,ij}\frac{\partial \hat{u}_{p,i}}{\partial x_j} = 0 \quad (20)$$

where the subgrid covariance is $q_{gp,SGS} = \widehat{u_{p,k}u_{g,k}} - \hat{u}_{p,k}\hat{u}_{g,k}$. To first order, the drag force term can be neglected and $\Pi_{\delta\theta_p}$ can be modeled by: $\Pi_{\delta\theta_p} \approx \mathcal{T}_{p,ij}\partial\hat{u}_{p,i}/\partial x_j$ with the SGS tensor modeled by Eq. (18). This model ensures that the correlated energy dissipated by subgrid effects is fully transfered into RUE to be finally dissipated by friction with the fluid.

### Comparison of gas flow without particles

Before discussing results for the dispersed phase, the accuracy of the LES solver for the gas phase is evaluated by computing the flow without particles and comparing it to the same data provided in Borée *et al.* (2001). The grid used with the code AVBP is presented in Fig. 2 and some parameters of the simulation are summarized in Table 1.

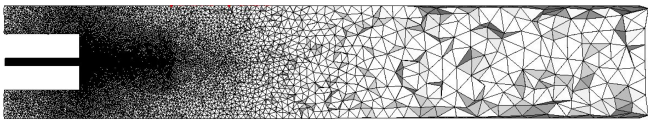

Figure 2: Geometry of the computational domain. Grid elements used: tetrahedra.

| | |
|---|---|
| Grid type | Tetrahedra |
| Number of cells / nodes | 2,058,883 / 367,313 |
| Time step ($\mu$s) / CFL | 3.2 / 0.7 |
| Averaging time (s) / Iterations | 1.03 / 320,000 |
| LES model | Smagorinsky |
| Wall model | Law-of-the-wall |

Table 1: Summary of parameters and models used in AVBP for the gas-flow computation without particles.

A typical snapshot of the velocity field (modulus) in the central plane is displayed in Fig. 3. The figure shows the complex structure of the recirculating flow: on the axis, the flow is recirculating down to $z = 200$ mm. On the sides of the channel, the flow also separates from $z \approx 50$ mm to $z \approx 400$ mm.

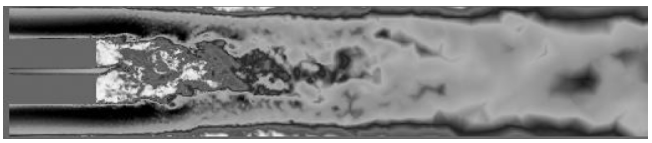

Figure 3: Instantaneous field of velocity modulus. Maximum value (black): 6 m/s. Minimum value (white): 0 m/s.

In Figs 4 to 7, the radial profiles (averaged in the azimuthal direction) of mean and RMS velocities obtained by AVBP are compared with the experimental values at 7 stations of the $z$ axis ($z = 3, 80, 160, 200, 240, 320$ and $400$ mm). The LES solver captures most of the flow physics: the axial mean and RMS velocities (Fig. 4 and 5) agree with the measurements. The length of the recirculation zone (evidenced by the negative values of axial velocities on the axis) is well predicted. In the coflow, the RMS values predicted by LES are too low because no turbulence is injected at the inlet of the domain for these computations.

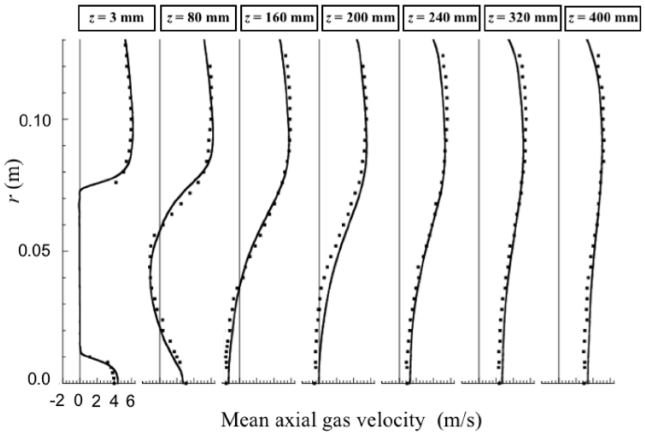


Figure 4: Radial profiles of mean axial gas velocities at 7 stations along $z$ axis. Symbols: experiment; solid line: AVBP.

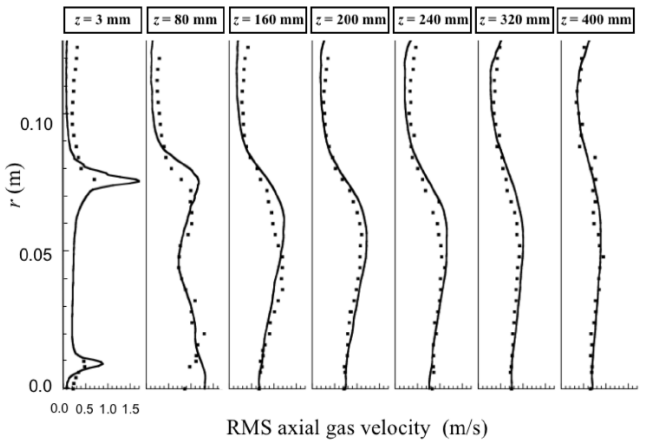


Figure 5: Radial profiles of RMS axial gas velocities at 7 stations along $z$ axis. Symbols: experiment; solid line: AVBP.

The mean radial velocity levels (Fig. 6) remain small (less than 1 m/s) and the LES code captures the radial velocity fields correctly (Fig. 7). The particle mean stagnation point (around $z = 160$ mm) is a delicate zone where the AVBP solver has some difficulties. The source of this problem is the exact position of the stagnation point: any small mismatch in this position leads to large changes in profiles measured around this point. Upstream and downstream of this point, the agreement is very good.

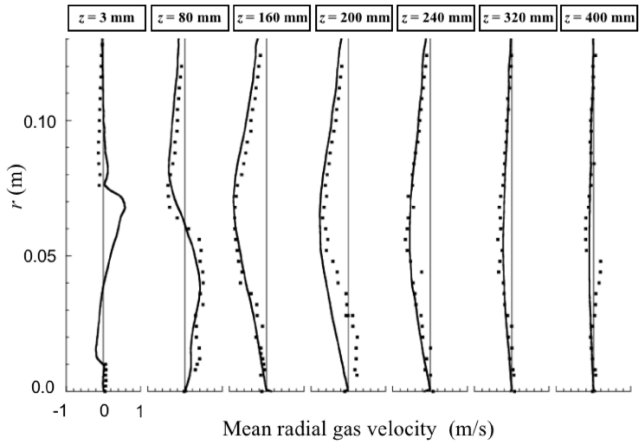


Figure 6: Radial profiles of mean radial gas velocities at 7 stations along $z$ axis. Symbols: experiment; solid line: AVBP.

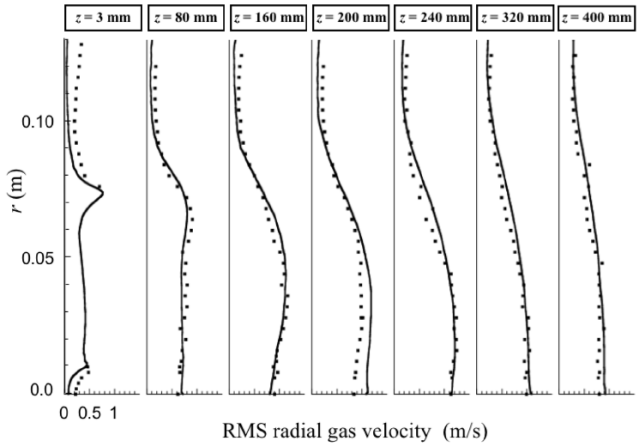


Figure 7: Radial profiles of RMS radial gas velocities at 7 stations along $z$ axis. Symbols: experiment; solid line: AVBP.

The code exhibits an overall good agreement with experimental results. This indicates that tests for the dispersed phase can be performed with reasonable confidence.

### Results for two-phase flow cases

This section presents the results for the 22 percent mass loading of the central jet, obtained with two different computations summarized in Table 2[1]. The grid and the time step used are presented in Table 1. In all computations presented here, the injected particles have a size of 60 microns. Separated studies which are not reported here, using another Lagrangian solver and multidisperse particles or 60 microns particles have shown that using a monodisperse distribution of size was very close to the 22 percent case of Borée *et al.* (2001) and was sufficient to capture both the mean flow effects on the gas (through two-way coupling) and the dynamics of the 60 microns class.

[1]For these runs, the RUM model is not used and the $\widehat{\delta\theta}_p$ term in Eq. (10) is set to zero.

| | EE | EL |
|---|---|---|
| Averaging time (s) | 0.64 | 0.80 |
| Particle mean speed | Exp. profile | Exp. profile |
| Turbulent fluctuations | Zero | White noise (12%) |
| Particle distribution | Exp. profile | Homogeneous |

Table 2: Summary of parameters and models used for the particle injection (22 percent mass loading computation). The particles are injected in the central tube.

An essential part of these LES is the introduction of the particles in terms of position and velocity. The injection planes are not the same for both approaches (Fig. 8). The methodologies used to inject the particles are also different to evaluate their impact on results. In EE, both the mass loading and the mean velocity imposed in the injection plane ($z = -200$ mm) are the ones measured experimentally at $z = 3$ mm. No turbulent fluctuations are introduced. In the EL formulation, the mass loading is homogeneous over the injection section and the injection speed profile is also the experimental one measured at $z = 3$ mm. In the EL formulation, a white noise (amplitude of the order of 12 percent of the mean velocity) is added to the particle mean velocity profiles to match experimental measurements at $z = 3$ mm.

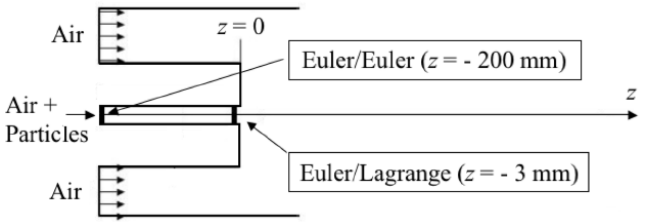


Figure 8: Injection position for particles.

The velocity fields for the gas phase change when the particles are injected but these effects are limited and are not discussed here. Figures 9 to 12 show velocity fields for particles obtained with both approaches along with the measurements of Borée. The agreement between the experiments and the two LES sets of data is good. An interesting result is that EE (solid line) and EL (dashed line) provide similar results showing that the EE approach is able to reproduce the mean-flow properties predicted by the EL computation. On the other hand, Figs. 10 and 12 show that EL formulation predicts particle RMS velocity more precisely. This is consistent with the fact that, when no RUM model is used, the EE approach underestimates turbulent fluctuations of particle velocity. Recent studies by Riber *et al.* (2006) have shown that when these contributions are considered, particle velocity fluctuations are correctly predicted.
A convenient way to look at the results is to consider the central $z$ axis of the configuration: a critical zone is the stagnation point for the gas located around $z = 160$ mm. This is also a zone where particles accumulate and must stop before

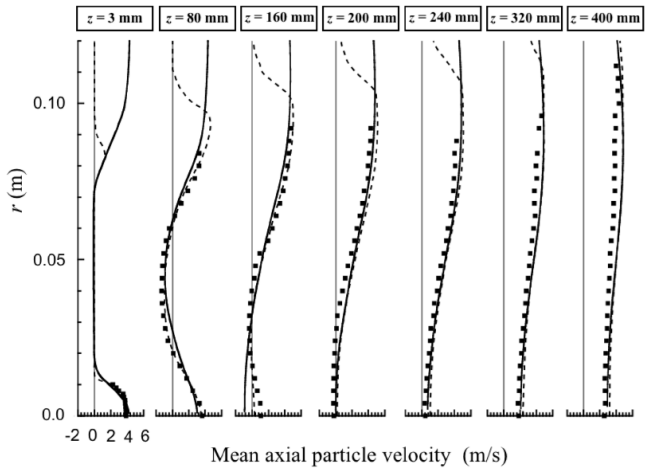


Figure 9: Radial profiles of mean axial particle velocities at 7 stations along $z$ axis. Symbols: experiment; solid line: EE; dashed line: EL.

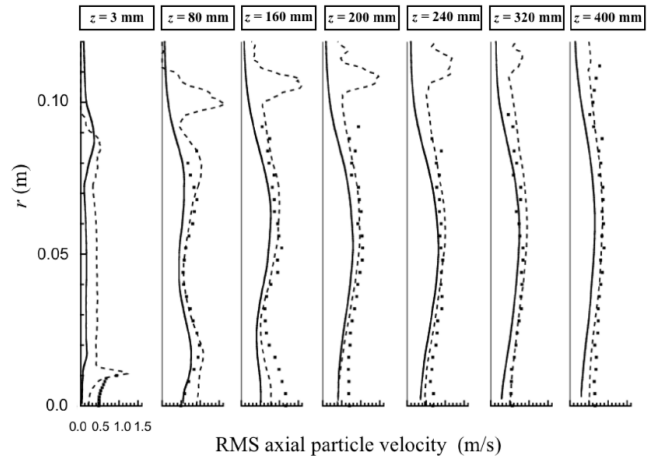


Figure 10: Radial profiles of RMS axial particle velocities at 7 stations along $z$ axis. Symbols: experiment; solid line: EE; dashed line: EL.

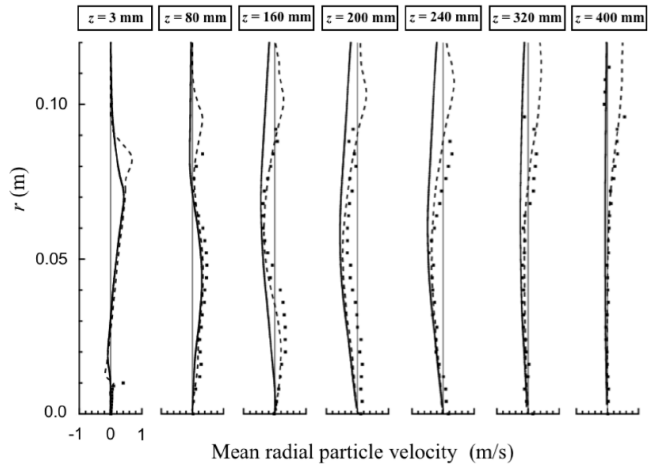


Figure 11: Radial profiles of mean radial particle velocities at 7 stations along $z$ axis. Symbols: experiment; solid line: EE; dashed line: EL.

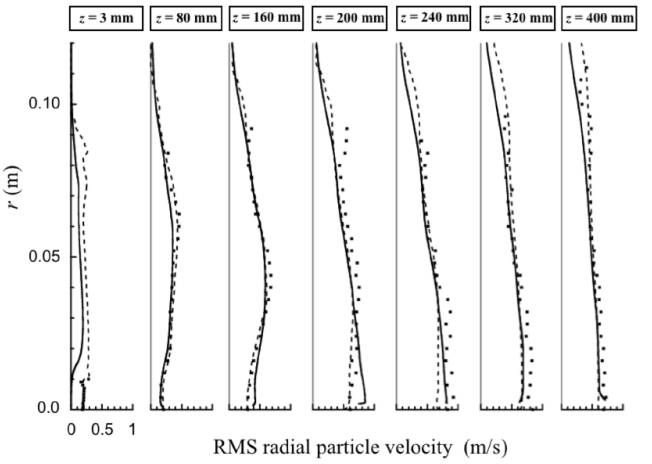


Figure 12: Radial profiles of RMS radial particle velocities at 7 stations along $z$ axis. Symbols: experiment; solid line: EE; dashed line: EL.

turning around to escape from the recirculating flows by the sides. Figure 13 shows field of local volume fraction of solid particles for the EE computation. Local droplet accumulation is also observed upstream of the stagnation point within the central jet.

Figure 13: Instantaneous volume fraction in the central plane from Euler-Euler simulation.

This can be quantified by plotting mean velocities along the axis for the gas (Fig. 14) and for the solid particles (Fig. 15). On this axis, both AVBP results match but are slightly off the experimental results. The cause of this discrepancy was investigated through various tests and was identified as the absence of turbulence injected on the gas phase in the inner jet: a direct verification of this effect is that in both computations (EE: solid and EL: dashed lines), the gas and the particle velocities in the central duct increase between $z = -200$ and $z = 0$ mm, indicating that the flow is relaminarizing. This also demonstrates the importance of injecting not only the proper mean profile for the gas velocity but also fluctuations with a reasonably well-defined turbulent spectrum. Additional tests also reveal that the injection of white noise on the particle velocities has a very limited effect on the results.

Figures 16 and 17 display axial profiles of RMS velocities for the gas and the particles. These plots confirm that the position where the maximum levels of gas and particle turbulence are found on the axis is shifted towards the jet inlet and is too intense for both computations.

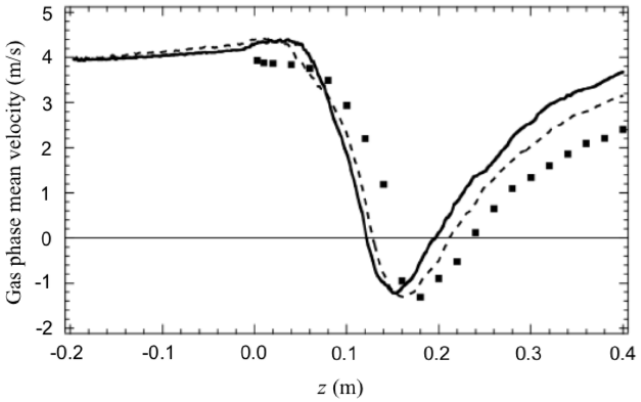


Figure 14: Axial profiles of mean gas velocities. Symbols: experiment; solid line: EE; dashed line: EL.

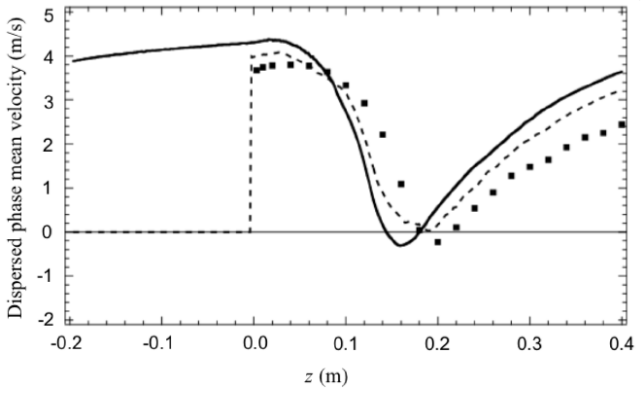


Figure 15: Axial profiles of mean particle velocities. Symbols: experiment; solid line: EE; dashed line: EL.

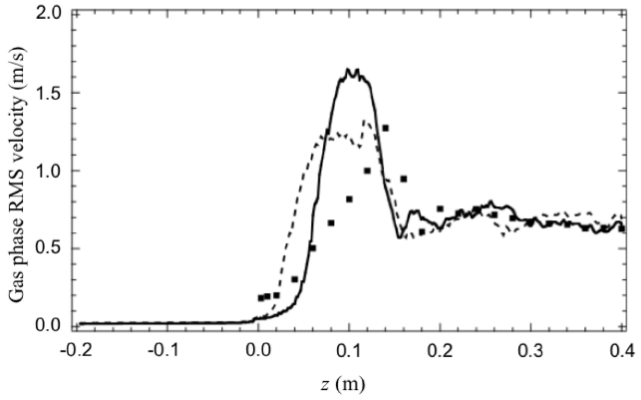


Figure 16: Axial profiles of RMS gas axial velocities. Symbols: experiment; solid line: EE; dashed line: EL.

## Analysis of code scalability

In terms of code implementation EE techniques are naturally parallel because the flow and the droplets are solved using the same solver (Kaufmann 2004). On the other hand, the EL approach is not well-suited to parallel computers since two different solvers must be coupled, which increases the complexity of the implementation on a parallel computer. In this case, two methods can be used for LES:

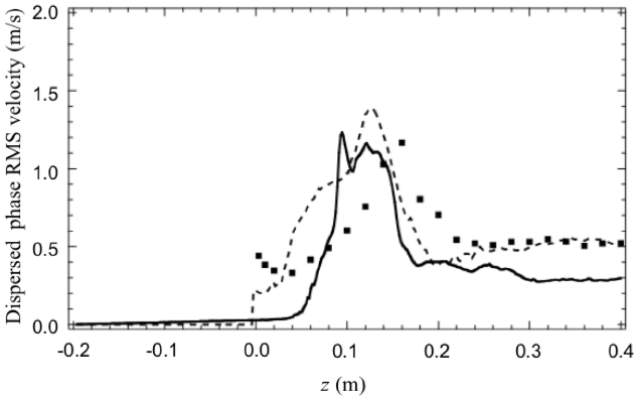


Figure 17: Axial profiles of RMS particle axial velocities. Symbols: experiment; solid line: EE; dashed line: EL.

1. Task parallelization in which some processors compute the gas flow and others compute the droplets flow.

2. Domain partitioning in which droplets are computed together with the gas flow on geometrical subdomains mapped on parallel processors. Droplets must then be exchanged between processors when leaving a subdomain to enter an adjacent domain.

For LES, it is easy to show that only domain partitioning is efficient on large grids because task parallelization would require the communication of very large three-dimensional data sets at each iteration between all processors. However, codes based on domain partitioning are difficult to optimize on massively parallel architectures when droplets are clustered in one part of the domain (typically, near the fuel injectors). Moreover, the distribution of droplets may change during the computation: for a gas turbine reignition sequence, for example, the chamber is filled with droplets when the ignition begins thus ensuring an almost uniform droplet distribution; these droplets then evaporate rapidly during the computation, leaving droplets only in the near injector regions. This leads to a poor speedup on a parallel machine if the domain is decomposed in the same way for the entire computation. As a result, dynamic load balancing strategies are required to redecompose the domain during the computation itself to preserve a high parallel efficiency (Ham *et al.* 2003).

In this section, the scalability of the EL model is analyzed by means of two basic parameters used to measure the efficiency of parallel implementation: the speedup and the reference single-phase CPU time ratio. The former is defined as the ratio between the CPU time of a simulation with 1 processor and the CPU time of a simulation with a given number of processors, $N_{procs}$:

$$Speedup = \frac{T_{run}(1)}{T_{run}(N_{procs})} \, . \tag{21}$$

The latter is defined as the ratio between the CPU time of a simulation with a given number of procs and the CPU time of the reference single-phase simulation with 1 processor:

$$CPU\ time\ ratio = \frac{T_{run}(N_{procs})}{T_{single-phase}(1)}\ . \qquad (22)$$

Note that the speedup of the EE model can be considered as good as the single-phase computation since the dispersed phase uses the same parallelization applied to the gaseous phase. The EE formulation additional cost is of the order of $80$ percent for this test case since the computational cost does not depend on the number of particles.

A scalability study of the EL simulation has been performed in a CRAY XD1 supercomputer at CERFACS for a number of processors up to 64. Table 3-4 and Figs. 18-19 summarize these results for this case (inner jet mass loading of 22 percent) with a total number of particles present in the domain of the order of $600{,}000$.

| $N_{procs}$ | 1 | 2 | 4 | 8 | 16 | 32 | 64 |
|---|---|---|---|---|---|---|---|
| Ideal scaling | 1 | 2 | 4 | 8 | 16 | 32 | 64 |
| Single-phase | 1 | 2.01 | 4.06 | 8.2 | 16.2 | 32.7 | 62.5 |
| Two-phase EL | 1 | 1.92 | 3.85 | 7.4 | 13.3 | 22.9 | 34.9 |

Table 3: Summary of the speedup of the EL approach. Supercomputer: CRAY XD1.

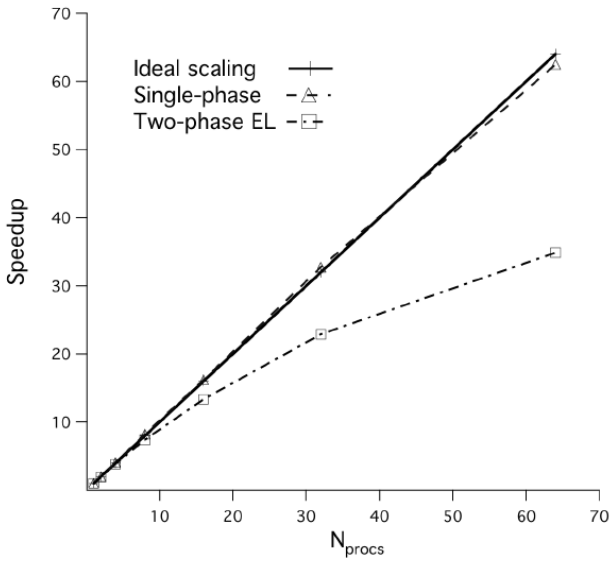


Figure 18: Speedup of the single-phase and the two-phase EL simulation. Supercomputer: CRAY XD1.

The drop of performances shown in Fig 18 is not related to large communications costs between processors as it might be thought at first sight but merely to the parallel load imbalance generated by the partitioning algorithm (Garcia *et al.* 2005). This effect can be observed by plotting the number of nodes, cells and particles presented in each processor. Figure 20 reports the number of nodes and cells presented per processor for a 32-partition simulation by using a recursive inertial bisection (RIB) partitioning algorithm. It shows an excellent load-balancing for the gaseous phase: all processors contains about the same number of cells ($\approx 64{,}500/$processor) and nodes ($\approx 13{,}000/$processor). On the other hand, Fig. 21 shows a huge particle load imbalance where one single processor contains almost half the total number of particles of the simulation. This increases significantly the memory requirements ($\approx$ 20 times the number of nodes) and the floating-point operations for this processor. This points out the need of dynamic load balancing for two-phase flow simulations with a Lagrangian approach, for example, by using multi-constraint partitioning algorithms which take into account particle loading on each processor (Ham *et al.* 2003).

| $N_{procs}$ | 1 | 2 | 4 | 8 | 16 | 32 | 64 |
|---|---|---|---|---|---|---|---|
| Single-phase | 1 | 0.50 | 0.25 | 0.12 | 0.06 | 0.030 | 0.016 |
| Two-phase EL | 1.05 | 0.54 | 0.27 | 0.14 | 0.08 | 0.046 | 0.030 |

Table 4: Summary of the CPU time ratios of the EL approach. Supercomputer: CRAY XD1.

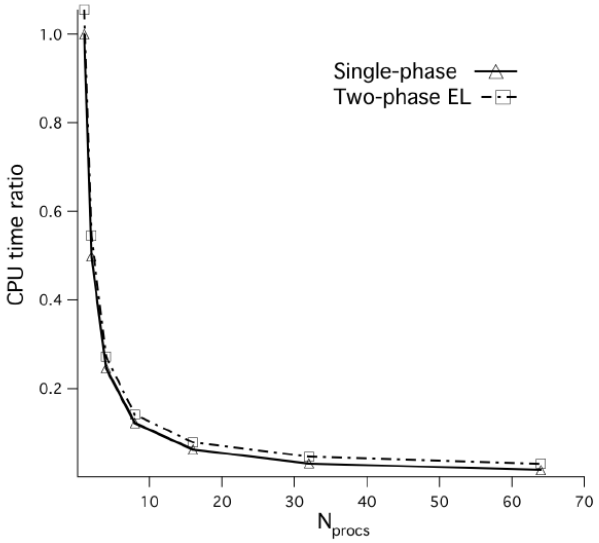


Figure 19: CPU Time ratio of the single-phase and the two-phase EL simulation. Supercomputer: CRAY XD1

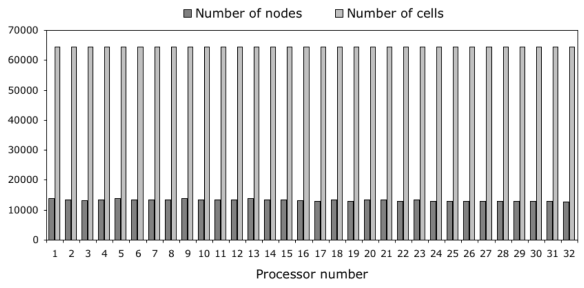


Figure 20: Number of cells and nodes per processor for a 32-partition by using a recursive inertial bisection (RIB) partitioning algorithm.

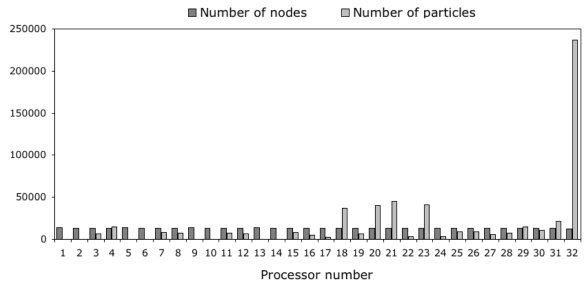


Figure 21: Number of nodes and particles per processor for a 32-partition by using a recursive inertial bisection (RIB) partitioning algorithm.

## Conclusions and perspectives

For the present test case (mass loading of 22 percent), the total number of particles present in the domain for the Lagrange codes is of the order of 600,000. For such a small number of particles, the computing power required by the Lagrangian solvers compared to the power required for the gas flow remains low: the additional cost due to the particles is small even with the load balancing problem observed when increasing the number of parallel processors. The EE formulation additional cost (of the order of 80 percent) is independent of the mass loading, so that, for such a dilute case, the EL formulations proved to be faster up to 64 processors. In terms of results quality, the EL and the EE results implemented into the AVBP solver are very close showing that both formulations lead to equivalent results in this situation. An important factor controlling the quality of the results is the introduction of turbulence on the gas flow in the injection duct: without these turbulent fluctuations, the results are not as good on the axis in terms of positions of the recirculation zones. In addition, the absence of RUV contribution considered in the present case evidences an underestimation of turbulent fluctuations for the EE results to be taken into account in future works. Future developments of the Lagrangian module of the AVBP solver will be devoted to the integration of a particle/mesh load balancing capabilities to improve scalability of the EL simulations.

## Acknowledgements

The help of Pr J. Borée in providing the experimental data and analyzing the results is gratefully acknowledged.

## References

Apte, S.V., Mahesh, K., Moin, P. & Oefelein, J.C. Large-eddy simulation of swirling particle-laden flows in a coaxial-jet combustor. International Journal of Multiphase Flow, Volume 29, 1311 – 1331 (2003).

Boivin, M., Simonin, O. & Squires, K. Direct numerical simulation of turbulence modulation by particles in isotropic turbulence. Journal of Fluid Mechanics, Volume 375, 235 – 263 (1998)

Boivin, M., Simonin, O. & Squires, K. On the prediction of gas-solid flows with two-way coupling using large eddy simulation. Physics of Fluids, Volume 12, Number 8, 2080 – 2090 (2000).

Borée, J., Ishima, T. & Flour, I. The effect of mass loading and inter-particle collisions on the development of the polydispersed two-phase flow downstream of a confined bluff body. Journal of Fluid Mechanics, Volume 443, 129 – 165 (2001)

Caraeni, D., Bergstrom, C. & Fuchs, L. Modeling of liquid fuel injection, evaporation and mixing in a gas turbine burner using large eddy simulation. Flow, Turbulence and Combustion, Volume 65, 223 – 244 (2000)

Chapman, S. & Cowling, T. The Mathematical Theory of Non-Uniform Gases. Cambridge Mathematical Library Edition. Cambridge University Press (1939) (digital reprint 1999)

Colin, O., Ducros, F., Veynante, D. & Poinsot, T. A thickened flame model for large eddy simulations of turbulent premixed combustion. Physics of Fluids, Volume 12, Number 7, 1843 – 1863 (2000)

Colin, O. & Rudgyard, M. Development of high-order Taylor-Galerkin schemes for unsteady calculations. Journal of Computational Physics, Volume 162, Number 2, 338 – 371 (2000)

Druzhinin, O.A. & Elghobashi, S. On the decay rate of isotropic turbulence laden with microparticles. Physics of Fluids, Volume 11, Number 3, 602 – 610 (1999)

Fede, P. & Simonin, O. Numerical Study of Subgrid Fluid Turbulence Effects on the Statistics of Heavy Colliding Particles. Physics of Fluids, Volume 18, 045103 (17 pages) (2006)

Février, P. & Simonin, O. Development and Validation of a Fluid and Particle Turbulent Stress Transport Model in Gas-Solid Flows. Proc. 9th Workshop on Two-Phase Flow Predictions, Merseburg, M. Sommerfeld (Editor), 77 – 85 (1999)

Février, P., Simonin, O. & Squires, K. Partitioning of particle velocities in gas-solid turbulent flows into a continuous field and a spatially uncorrelated random distribution: Theoretical formalism and numerical study. Journal of Fluid Mechanics, Volume 533, 1 – 46 (2005)

García, M., Sommerer, Y., Schönfeld T. & Poinsot, T. Evaluation of Euler-Euler and Euler-Lagrange strategies for Large-Eddy Simulations of turbulent reacting flows. ECCOMAS thematic conference on computational combustion, Lisbon, Portugal (2005)

Gatignol, R. The Faxén formulae for a rigid particle in an unsteady non-uniform Stokes flow. Journal de mécanique théorique et appliquée, Volume 1, Number 2, 143 – 160 (1983)

Ham, F., Apte, S., Iaccarino, G., Wu, X., Herrmann, M., Constantinescu, G., Mahesh, K. & Moin, P. Unstructured LES of reacting multiphase flows in realistic gas turbine combustors.

In Annual Research Briefs. Center for Turbulence Research, NASA Ames/Stanford Univ, 139 – 160 (2003)

Ishima, T., Borée, J., Fanouillère, P. & Flour, I., Presentation of a two phase flow data based obtained on the flow loop Hercule. Proc. 9th Workshop on Two-Phase Flow Predictions, Merseburg, M. Sommerfeld (Editor), 3 – 18 (1999)

Kaufmann, A., Simonin, O., Cuenot, B., Poinsot, T. & Helie, J. Dynamics and dispersion in 3D unsteady simulations of two phase flows. In Supercomputing in Nuclear Applications. Paris: CEA. (2003)

Kaufmann, A. Vers la simulation des grandes échelles en formulation Euler/Euler des écoulements réactifs diphasiques. PhD thesis (2004)

Kaufmann, A., Hélie, J., Simonin, O., & Poinsot, T. Comparison between Lagrangian and Eulerian Particle Simulations Coupled with DNS of Homogeneous Isotropic Decaying Turbulence. Proceedings of the Estonian Academy of Sciences. Engineering, Volume 11, Number 2, 91 – 105 (2005)

Maxey, M. & Riley, J. Equation of motion for a small rigid sphere in a nonuniform flow. Physics of Fluids, Volume 26, Number 4, 883 – 889 (1983)

Moin, P., Squires, K., Cabot, W. & Lee, S. A dynamic subgrid-scale model for compressible turbulence and scalar transport. Physics of Fluids A, Volume 3, Number 11, 2746 – 2757 (1991)

Moreau, M., Bédat, B. & Simonin, O. A priori testing of subgrid stress models for euler-euler two-phase LES from euler-lagrange simulations of gas-particle turbulent flow. In 18th Annual Conference on Liquid Atomization and Spray Systems. ILASS Americas. (2005)

Moureau, V., Lartigue, G., Sommerer, Y., Angelberger, C., Colin, O. & Poinsot, T. High-order methods for dns and les of compressible multicomponent reacting flows on fixed and moving grids. Journal of Computational Physics, Volume 202, Number 2, 710 – 736 (2005)

Poinsot, T. & Veynante, D. Theoretical and numerical combustion. R.T. Edwards, 2nd edition (2005)

Reeks, M. W. On a kinetic equation for the transport of particles in turbulent flows. Physics of Fluids A, Volume 3, 446 – 456 (1991)

Riber, E., Moreau, M., Simonin, O. & Cuenot, B. Towards large eddy simulations of non-homogeneous particle laden turbulent gas flows using euler-euler approach. In 11th Workshop on Two-Phase Flow Predictions. Merseburg, Germany. (2005)

Riber, E., Moreau, M., Simonin, O. & Cuenot, B. Development of Euler-Euler LES Approach for Gas-Particle Turbulent Jet Flow. In Proceedings of Symposium Fluid-Particle Interactions in Turbulence. ASME Joint U.S. European Fluids Engineering Summer Meeting. Miami, FEDSM2006-98110 (2006)

Roux, S., Lartigue, G., Poinsot, T., Meier, U. & Bérat, C. Studies of mean and unsteady flow in a swirled combustor using experiments, acoustics analysis and large eddy simulations. Combustion and Flame, Volume 141, 40 – 54 (2005)

Schiller, L. & Nauman, A. A drag coefficient correlation. V.D.I. Zeitung, Volume 77, 318 – 320 (1935)

Schmitt, P., Poinsot, T., Schuermans, B. & Geigle, K. Large-eddy simulation and experimental study of heat transfer, nitric oxide emissions and combustion instability in a swirled turbulent high pressure burner. Journal of Fluid Mechanics, Volume 570, 17 – 46 (2007)

Selle, L., Lartigue, G., Poinsot, T., Koch, R., Schildmacher, K.-U., Krebs, W., Prade, B., Kaufmann, P. & Veynante, D. Compressible large-eddy simulation of turbulent combustion in complex geometry on unstructured meshes. Combustion and Flame, Volume 137, Number 4, 489 – 505 (2004)

Simonin, O., Février, P., & Laviéville, J. On the Spatial Distribution of Heavy-Particle Velocities in Turbulent Flow : from Continuous Field to Particulate Chaos Journal of Turbulence, Volume 3, 040 (2002)

Vermorel, O., Bédat, B., Simonin, O. & Poinsot, T. Numerical study and modelling of turbulence modulation in a particle laden slab flow. Journal of Turbulence, Volume 4, Number 025, 1 – 39 (2003)

Vreman, B., Geurts, B. & Squires, K. Subgrid modeling in les of compressible flow. Applications Scientific Research, Volume 54, 191 – 203 (1995)

Wang, Q. & Squires, K. Large eddy simulation of particle-laden turbulent channel flow . Physics of Fluids, Volume 8, Number 5, 1207 – 1223 (1996)

Yamamoto, Y., Potthoff, M., Tanaka, T., Kajishima, T. & Tsuji, Y. Large-eddy simulation of turbulent gas-particle flow in a vertical channel: effect of considering inter-particle collisions. Journal of Fluid Mechanics, Volume 442, 303 – 334 (2001)

Yoshizawa, A. Statistical theory for compressible turbulent shear flows, with the application to subgrid modeling. Physics of Fluids, Volume 29, Number 7, 2152 – 2164 (1986)